Water Science & Technology

IWA PUBLISHING

Water Science & Technology Vol 85 No 7, 2208 doi: 10.2166/wst.2022.102

Adsorption of methyl orange on ZnO supported by seawater-modified red mud

Chun-Lei Qiao, Yan-Ming Xu, Yue Yin, Yu-Xing Xu, Yi-Hua Xiao and Chang-Qing Liu*

School of Environmental & Municipal Engineering, Qingdao University of Technology, Qingdao 266033, China
*Corresponding author. E-mail: lcqlfy@163.com

C-QL, 0000-0002-6114-3238

ABSTRACT

In this study, a novel adsorbent (SRM-ZnO) was prepared using zinc oxide supported on red mud in a seawater medium and was used for the adsorption of methyl orange (MO). It is expected to solve the recycling of red mud and prepare an economical adsorbent with high efficiency to adsorb dye wastewater. Material composition and morphology analyses showed that hydrotalcite compounds were attached on the surface of SRM-ZnO. The hydrotalcite compounds can increase the surface area of the modified red mud and thus increase the adsorption capacity of MO. The adsorption of MO dye on modified red mud conforms to the Temkin isotherm model and pseudo-second-order kinetic model. The adsorption behavior mainly includes physical interaction, supplemented with chemical interactions. Result also found that the adsorption of MO on SRM-ZnO is a spontaneous exothermic process.

Key words: adsorption, methyl orange, red mud, seawater, zinc oxide

HIGHLIGHTS

- A novel adsorbent was prepared using ZnO supported on red mud in seawater.
- Hydrotalcite compounds formed on the surface of SRM-ZnO can improve adsorbing capacity.
- The adsorption complies with the Temkin isotherm model and pseudo-second-order kinetic model.
- The adsorption is mainly physisorption, supplemented with chemical adsorption.

GRAPHICAL ABSTRACT

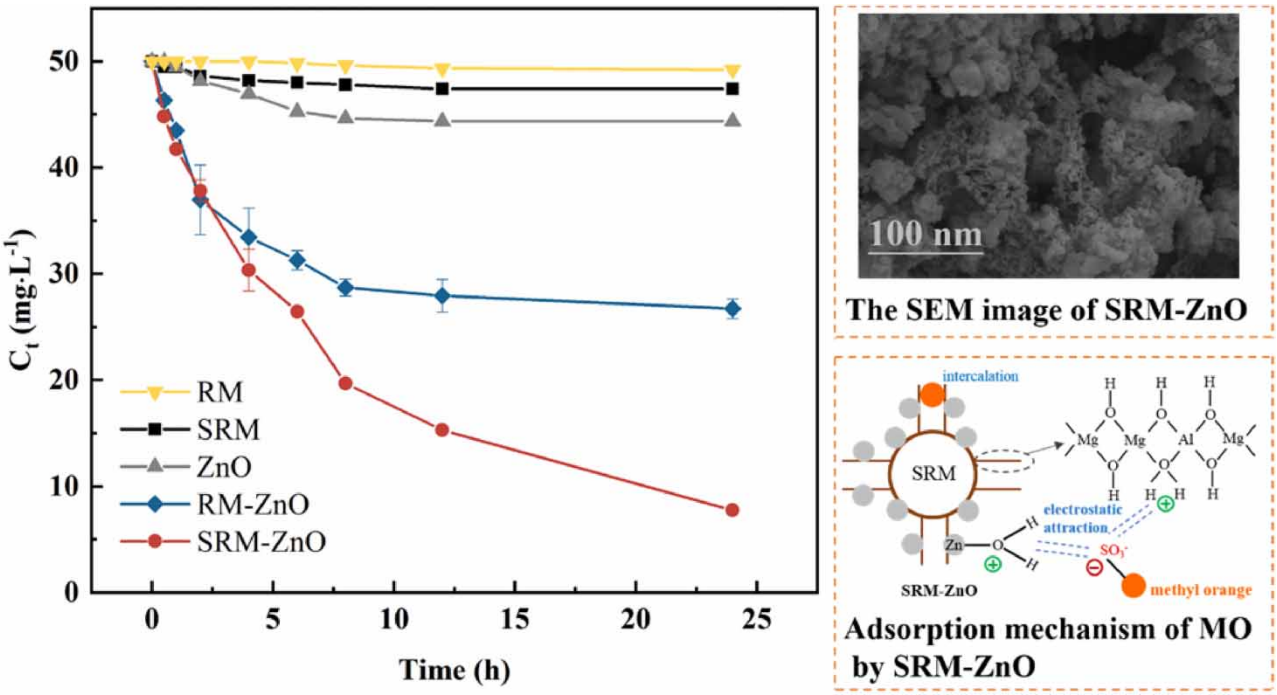

INTRODUCTION

Nowadays, large quantities of dye effluents produced from textile, paper, printing, leather, plastics, leather tanning industrial activities are released into environment, leading to harmful effects on the aquatic organisms and human health (Gupta & Saleh 2013; Dil *et al.* 2016). It is reported that around one thousand tons of dyes are discharged in to the environment only as textile waste annually (Ajmal *et al.* 2014). Therefore, it is urgent to find efficient ways to treat these toxic dye effluents efficiently and economically. A wide range of technologies including adsorption, biological treatment, flotation, ozone oxidation, electrochemical, photodegradation, and chemical coagulation have been used to treat dye-rich wastewaters. Among the various treatment technologies, adsorption is attracting attention owing to its high efficiency and low cost. However, the adsorption performance of the adsorbents and the constant supply of materials determine whether the adsorption process will be successful or not (Ghaedi *et al.* 2012). Dyes can be classified as anionic, cationic and non-ionic (Fernandes *et al.* 2020). Methyl orange (MO) is a kind of anionic dye on account of the deprotonation of sulfonate on MO molecule in the aqueous solution with a complex chemical formula of $C_{14}H_{14}N_3SO_3Na$ shown in Figure 1 (Azam *et al.* 2020). MO is commonly present in effluent discharges from the textile, printing, paper manufacturing, food, and pharmaceutical industries and research laboratories (Haque *et al.* 2010). In this work, MO was used as a target organic pollutant representative of anionic dyes to explore the dye removal capacity of adsorbents. The selection of MO is of typical in the treatment of anionic dye effluents because MO is toxic and difficult to be adsorbed (Fernandes *et al.* 2020).

In recent years, metal oxide nanoparticles have been commonly used as adsorbents to treat dye wastewater due to their high surface area and strong physical and chemical effects on the adsorption of dye effluents. Zinc oxide (ZnO) is a kind of common metal oxide nanoparticle as adsorbent with low cost, high chemical stability, harmlessness to the environment, and high regeneration capacity (Kataria *et al.* 2016). It also has a positive charge at neutral pH with an isoelectric point (IEP) in the range from 9.3 to 9.8, indicating its adsorption potential for anionic dye MO as the MO molecules, which are negative in aqueous solution were easily adsorbed onto positive surfaces under the action of electrostatic force (Kosmulski 2004). Several methods have been used to synthesize ZnO, such as precipitation method (Rodrıguez-Paéz *et al.* 2001), indirect electrodeposition method (Kanade *et al.* 2006), sol-gel assisted hydrothermal method (Zhao *et al.* 2014), ultrasonication (Ma *et al.* 2015), sonochemical method (Chen *et al.* 2001), and mechanochemical method (Ao *et al.* 2006). From these, the precipitation method was selected to synthesize ZnO in this study for its advantage of simple operation. In addition,

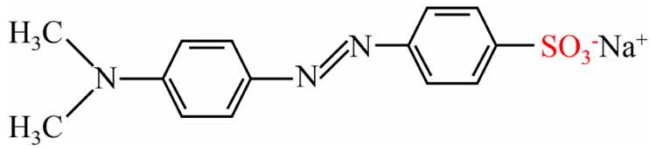

Figure 1 | Chemical structure of methyl orange.

the precursor of $Zn(OH)_2$ with layered structure was obtained by precipitation method, and anions (NO_3^-, Ac^-, SO_4^{2-}) would be inserted into the layer and released during calcination, resulting in larger pores of ZnO (Hou *et al.* 2012). However, ZnO nanoparticles (NPs) tend to aggregate in aqueous solution and are difficult to separate and recycle due to their high colloid stability (Keller *et al.* 2010; Zhang *et al.* 2018). Nowadays, there are two approaches to solve this problem and improve the adsorption capacity of ZnO. On one hand, methods to selectively control the size, shape, and organization of materials have been studied recently, such as flower-shaped ZnO NPs (Hou *et al.* 2012), hierarchical hollow structure ZnO (Lan *et al.* 2014), hierarchical porous ZnO microspheres (Lei *et al.* 2017), 3D hierarchical PbS/ZnO microspheres (Liu *et al.* 2020), ZnO hollow microspheres (Wang *et al.* 2013), etc. On the other hand, porous bodies with a larger surface area are used to load with ZnO NPs, which may change the adsorbent morphology and increase the available adsorption sites of adsorbent (Madan *et al.* 2019).

Red mud is the waste of the alumina production process with a large specific surface area and adsorption capacity for anionic dyes (Namasivayam & Arasi 1997). Some alumina refineries have used seawater to neutralize red mud by precipitation of hydrotalcite, which can increase the specific surface area of red mud. Palmer & Frost (2009) found that the process of treating red mud with seawater facilitated a significant reduction in dissolved metal concentrations, which could improve the safety and reliability of adsorption because the metals in red mud would not cause secondary pollution to water again. In addition, neutralization of red mud by seawater (SRM) could increase the settling rates due to agglomerate consolidation, which is conducive to the separation of adsorbent and solution (Palmer *et al.* 2009). At present, studies on SRM have been reported, while few studies have been conducted on the applications of SRM on the adsorption of dye. Therefore, the present work aims to use SRM as substrates and ZnO NPs were deposited on their surfaces to synthesize adsorbents of SRM-ZnO and RM-ZnO. In contrast with RM-ZnO, the prepared SRM-ZnO exhibited stronger adsorption capacity of MO in aqueous solution. SRM-ZnO was characterized via scanning electron microscopy (SEM), energy dispersive spectroscopy (EDS), and X-ray diffraction (XRD) analysis. In addition, the influences of pH, dosage, and anions on the adsorption of SRM-ZnO on MO were investigated to evaluate the adsorption performance and analyze the mechanism of the adsorption.

MATERIALS AND METHODS

Materials

Red mud was provided from an electrolytic aluminium factory in China, and seawater was obtained from Qiangdao, China. The major chemical composition of red mud is presented in Table 1 and the main parameters of raw seawater are presented in Table 2 (Song *et al.* 2011). There may be complexation of DOC with Zn^{2+} during the preparation of adsorptions, which could increase the solubility of Zn^{2+} and prevent the conversion of Zn^{2+} from dissolved fraction into particulate fractions. However, it can be seen from Table 2 that the value of COD_{Mn} is low, so the value of DOC is also low and has little influence on the morphological transformation of Zn^{2+} (Shafer *et al.* 1999; Chakraborty & Chakrabarti 2006). In addition, the other components in seawater has little negative impact on the preparation of adsorbent and raw seawater can be used directly in subsequent test. Zinc acetate dihydrate ($Zn(Ac)_2{\cdot}2H_2O$), sodium hydroxide (NaOH), hydrochloric acid (HCl), and MO were purchased from Sinopharm Chemical Reagent Co. LTD. Purified water (UNIQUE-R20 purification system, Xiamen, China) was used in the experiments.

Methods

Synthesis of SRM-ZnO, RM-ZnO, ZnO, and SRM

The synthesis method of ZnO supported by seawater modified red mud (SRM-ZnO) is as follows: a weight of 2 g of red mud sifted through 100 mesh was dispersed into 250 mL of seawater and left to age overnight to synthesize SRM. After that, 0.4 g of $Zn(Ac)_2{\cdot}2H_2O$ was dissolved in 5 mL purified water to produce a solution of $Zn(Ac)_2$. The prepared $Zn(Ac)_2$ solution was added into the mixture as described above under stirring on a magnetic stirrer to obtain a homogenous deposition of Zn^{2+} on

Table 1 | The major chemical composition of red mud

Compound Name	Conc.(%)
Fe_2O_3	43.142
Al_2O_3	22.179
SiO_2	12.615
Na_2O	12.379
TiO_2	5.945
CaO	2.214
P_2O_5	0.312
SO_3	0.311
ZrO_2	0.241
Cl	0.213
Cr_2O_3	0.200
MgO	0.120
MnO	0.075
K_2O	0.055

Table 2 | Main parameters of raw seawater

Parameters	Values
Turbidity (NTU)	10
Total alkalinity (mg/L)	200
COD_{Mn} (mg/L)	1.4–2.0
K^+ (mg/L)	393–405
Na^+ (mg/L)	11,042–11,451
Ca^{2+} (mg/L)	404–419
Mg^{2+} (mg/L)	1,289–1,325
Cl^- (mg/L)	18,906–19,565
SO_4^{2-} (mg/L)	2,342–2,396
PO_4^{3-} (mg/L)	0.17–0.20
pH	7.8–8.5

the surface of the solid. Then the pH of the solution was adjusted to above 10 to precipitate the Zn^{2+}. After being stirred for 1 h at room temperature, the precipitates were washed with deionized water, then dried at 80 °C and calcinated at 400 °C for 2 h. After the above steps, SRM-ZnO was fabricated for the adsorption experiments.

To further understand the adsorption mechanism of SRM-ZnO, we also synthesized ZnO supported by red mud (RM-ZnO), pure ZnO and SRM for reference. In a similar way, for the preparation of RM-ZnO, 2 g of sifted red mud was left in 250 ml purified water overnight and the solution with red mud was processed as above to obtain RM-ZnO. For the preparation of ZnO, a solution of 0.1 M $Zn(Ac)_2$ was added dropwise to 0.5 M of NaOH solution on the magnetic stirrer. After stirring for an hour, the white precipitates of $Zn(OH)_2$ formed were separated from the liquid, washed with deionized water, and then dried at 80 °C and calcinated at 400 °C for 2 h to obtain pure ZnO. For the preparation of SRM, 2 g of red mud was added into 250 mL of seawater overnight, and then the solids were calcinated at 400 °C for 2 h. The schematic diagram for synthesis process of SRM-ZnO, RM-ZnO, ZnO, and SRM is shown in Figure 2.

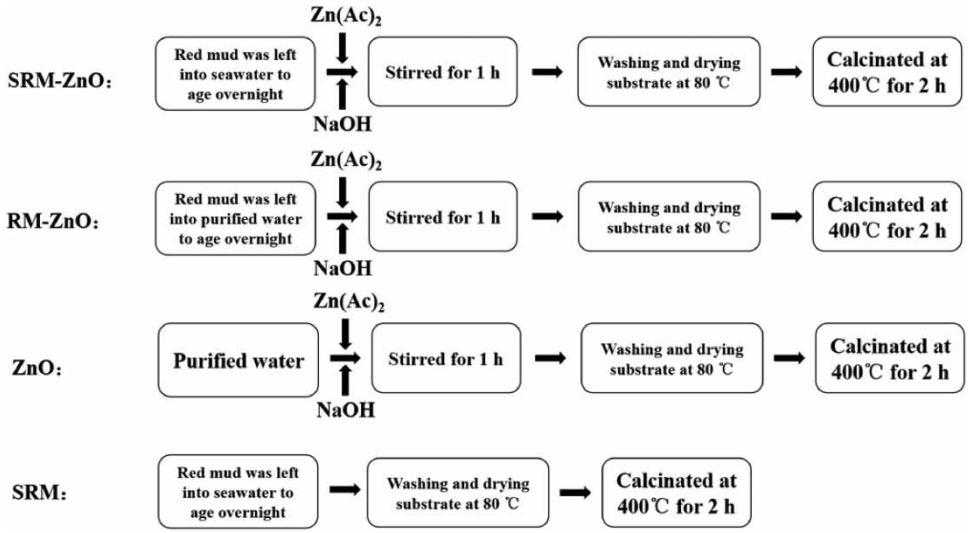

Figure 2 | Synthesis process of SRM-ZnO, RM-ZnO, ZnO, and SRM.

Adsorption of MO dye

A series of experiments were conducted in the batch form to investigate the effect of different factors in the adsorption of MO on adsorbents. All experiments were carried out using glass sample bottles. In a typical procedure, the desired dosage of adsorbent was dispersed into 25 ml MO solution under different condition such as pH, initial concentration of dyes, contact time, and temperature. The solution was vibrated in the dark at 180 rpm for the predefined time and then centrifuged for solid–liquid separation at 4,000 rpm for 5 min. The absorbency of MO over each sample in the supernatant was monitored using a UV-Vis spectrophotometer at a maximum wavelength of 463 nm. It was used to determine the residual concentration of MO. To achieve statistical soundness, experiments were replicated at least three times and the data were average values.

The quantity of MO adsorbed with adsorbents at equilibrium (q_e; mg·L^{-1}), the quantity of MO adsorbed with adsorbents at each time point (q_t; mg·L^{-1}), and the removal efficiency (R; %) were calculated by Equations (1)–(3), respectively.

$$q_e = \frac{(C_0 - C_e) \cdot V}{m} \tag{1}$$

$$q_t = \frac{(C_0 - C_t) \cdot V}{m} \tag{2}$$

$$R = \frac{C_0 - C_e}{C_0} \times 100\% \tag{3}$$

where C_o, C_t, and C_e (mg·L^{-1}) correspond to MO concentration of the contaminants at initial time, time t, and equilibrium time, respectively. On the other hand, V (L) and m (g) represent the volume of the solution and the mass of the adsorbents.

Modeling kinetic adsorption

The experimental kinetic data for the MO adsorption by SRM-ZnO were simulated with the pseudo-first-order model, pseudo-second-order model, and Elovich kinetics model as well as the intraparticle diffusion model, represented by Equations (4)–(7), respectively.

$$\log(q_e - q_t) = \log q_e - k_1 t \tag{4}$$

$$\frac{t}{q_t} = \frac{1}{k_2 q_e^2} + \frac{t}{q_e} \tag{5}$$

$$q_t = \left(\frac{1}{b}\right) \ln(ab) + \left(\frac{1}{b}\right) lnt \tag{6}$$

$$q_t = k_i t^{\frac{1}{2}} + I \tag{7}$$

where k_1 (h^{-1}), k_2 ($g{\cdot}mg^{-1}{\cdot}h^{-1}$), k_i ($mg{\cdot}g^{-1}{\cdot}h^{-1/2}$) are equilibrium rate constants of the pseudo-first-order, the pseudo-second-order, and intraparticle diffusion adsorption, respectively. The value of a ($mg{\cdot}g^{-1}{\cdot}h^{-1}$) is the initial adsorption rate and b ($g{\cdot}mg^{-1}$) is the desorption constant for a particular experiment, relating to the chemisorption activation energy. I ($mg{\cdot}g^{-1}$) value gives information regarding the thickness of boundary layer.

Modeling adsorption isotherm

The experimental data were simulated with Langmuir, Freundlich and Temkin isotherm models. The Langmuir model, which supposes that adsorbate can have a monolayer coverage on the adsorbent surface with energetically homogeneous sites and no interaction between the adsorbate molecules, can be expressed as Equations (8) and (9):

$$q_e = \frac{q_m \cdot K_L \cdot C_e}{1 + K_L \cdot C_e} \tag{8}$$

$$R_L = \frac{1}{K_L C_i} \tag{9}$$

where K_L and R_L are the Langmuir isotherm constants, and K_L represents equilibrium adsorption capacity. The adsorption nature is irreversible if $R_L = 0$, is favorable if $0 < R_L < 1$, is linear if $R_L = 1$, is unfavorable if $R_L > 1$.

The Freundlich model is mostly used to describe the multilayer adsorption on the non-uniform surface with the assumption that the adsorption energy is heterogeneously distributed, which is presented in Equation (10).

$$q_e = K_F C_e^{\frac{1}{n}} \tag{10}$$

where K_F and n are the Freundlich isotherm constants, and K_F represents equilibrium adsorption capacity. The heterogeneity factor (n) describes the suitability of adsorption, and the adsorption approach is irreversible if $1/n = 0$, is favorable if $0 < 1/n < 1$, is unfavorable if $1/n > 1$.

The Temkin model is applied to heterogeneous systems with the supposition that the adsorption binding energies are distributed uniformly and the fall in the heat of adsorption is linear rather than logarithmic with coverage by ignoring the extremely low and large value of concentrations.

$$q_e = \frac{RT}{b_T} \ln(K_T \cdot C_e) \tag{11}$$

where R is the general gas constant ($R = 8.3145\ J{\cdot}mol^{-1}{\cdot}K^{-1}$), T is the absolute temperature (K), b_T ($J{\cdot}mol^{-1}$) is the Temkin isotherm constant related to the heat of adsorption and K_T ($L{\cdot}g^{-1}$) is the Temkin isotherm equilibrium binding constant.

Absorbent characterization

X-ray diffraction (XRD) patterns were conducted from Smartlab 9 kw XRD of Nippon Science Corporation using Cu Kα radiation at 45 kV and 200 mA with a scanning range of 5°–80° and a step size of 0.02°. The morphology observation and elemental composition of the prepared adsorbents were detected with a scanning electron microscope (Zeiss Sigma300, SEM) with an acceleration voltage of 5 kV and an energy dispersive spectroscopy (Ultim Max 40, Oxford, EDS). The samples were previously loaded with a thin gold layer using a fine coater (ETD-2000).

RESULTS AND DISCUSSION

Absorbent characterization

To analyze crystallinity and phase components of as-prepared adsorbents, XRD measurements were carried out, and the patterns are illustrated in Figure 3(a). For the pattern of ZnO NPs, diffraction peaks at about $2\theta = 31.76°$, 34.40°, 36.24°, 47.54°, 56.60°, 62.84°, 67.96° could be nicely indexed to the (100), (002), (101), (102), (110), (103), (112) planes of hexagonal ZnO (JCPDS card no. 99-0111). These intense diffraction peaks demonstrate the formation of the highly pure and crystalline structure of the calcined nanoparticles. Meanwhile, it is also found that dimension of the ZnO crystallites is large for the sharp and symmetric peaks. It is noteworthy that part of the diffraction peaks of ZnO could be found in the patterns of RM-ZnO and

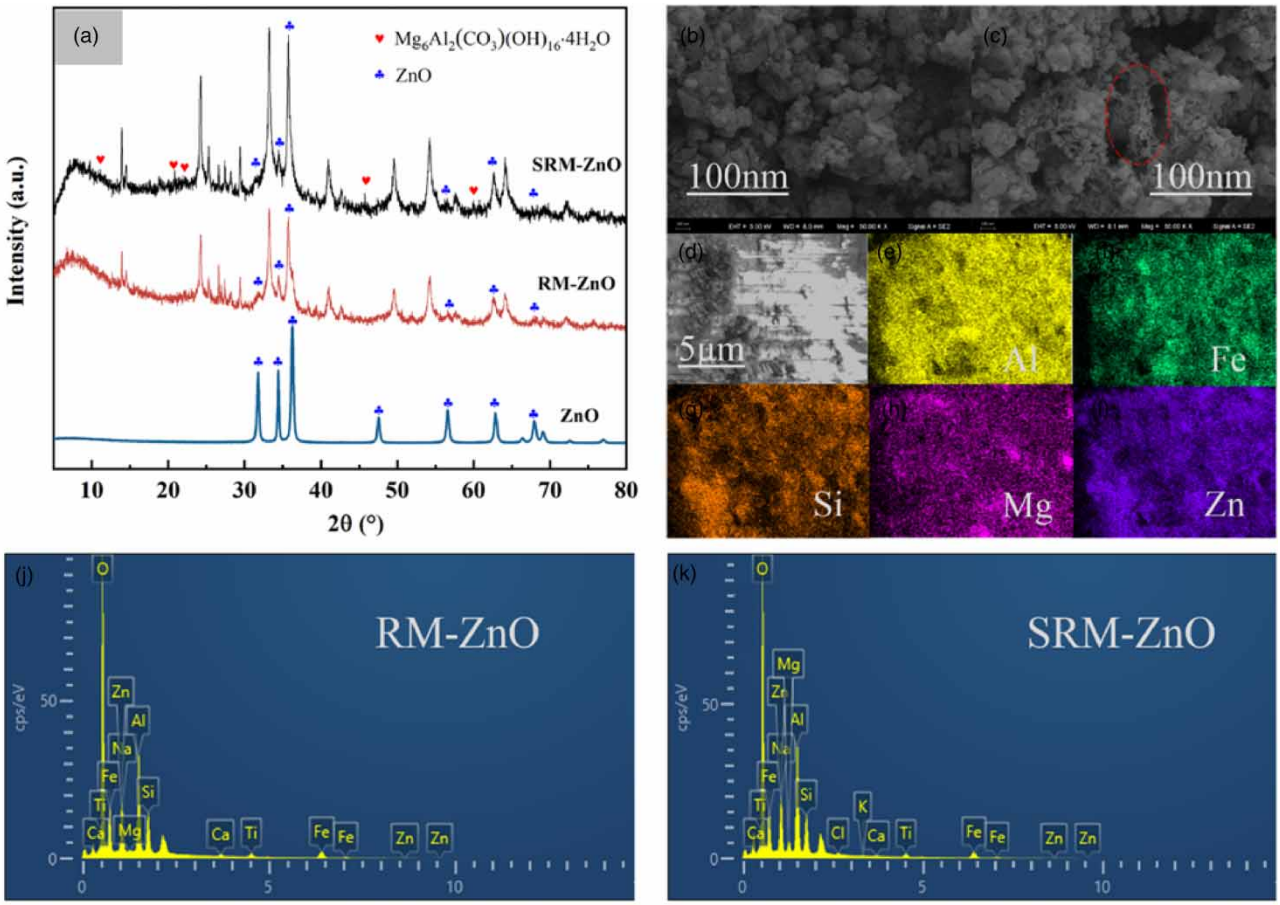

Figure 3 | XRD pattern of RM-ZnO, SRM-ZnO and ZnO (a), SEM images of RM-ZnO (b) and SRM-ZnO (c, d), EDS images of SRM-ZnO (e, f, g, h, i) and images with elemental spectra of RM-ZnO (j) and SRM-ZnO (k).

SRM-ZnO and these peaks are small and broad, suggesting that a thin layer of ZnO NPs has a good load on the surface of RM and SRM and the dimensions of ZnO crystallites loaded on RM and SRM are smaller, which can result in largger specific surface areas of RM-ZnO and SRM-ZnO. Additionally, few diffraction peaks corresponding to hydrotalcite ($Mg_6Al(CO_3)(OH)_{16}·4H_2O$) phase can be observed in the diffraction pattern of SRM-ZnO according to JCPDS card no.41.1428, indicating the formation of hydrotalcite on SRM-ZnO. According to previous studies, Mg^{2+} in seawater could react with CO_3^{2-}, OH^-, and $Al(OH)_4^-$ dissolved from RM in solution to precipitate hydrotalcite compounds (Johnston *et al.* 2010), and the reaction equation is shown as follows:

$$6Mg^{2+} + 2Al(OH)_4^- + 8OH^- + CO_3^{2-} + 4H_2O \rightarrow Mg_6Al_2(CO_3)(OH)_{16}·4H_2O \quad (12)$$

As can be seen in the pattern of SRM-ZnO, the intensity of these diffraction peaks concerning the hydrotalcite is low, and even some diffraction peaks corresponding to hydrotalcite cannot be detected. The phenomenon can be explained by the following reasons, (i) The hydrotalcite compounds were destroyed and converted to Al_2O_3 and MgO during calcination of 400 °C so that there were less hydrotalcite compounds in SRM-ZnO in solid state (Orthman *et al.* 2003); (ii) The concentration of OH^- and CO_3^{2-} decreased during the formation of hydrotalcite, which led to the fact that the pH dropped from 11 to 9 and it was difficult to dissolve Al from red mud into $Al(OH)_4^-$ in an alkalescent environment. Therefore, the crystallinity of hydrotalcite was poor and overshadowed by the sharper and more crystalline mineralogical phases in red mud (Palmer & Frost 2009).

To evaluate the textual morphology of surfaces of adsorbents, the micrographic images of RM-ZnO and SRM-ZnO were depicted by the scanning electron microscope (Zeiss Sigma300). Furthermore, the elemental compositions of these two

adsorbents were measured by EDS analysis. Typical SEM images of RM-ZnO and SRM-ZnO and the EDS spectra of SRM-ZnO are shown in Figure 3(b) and 3(c). Besides, Table 3 shows the weight percentage of Mg, Ca^{2+}, K^{+} and Zn elements in corresponding zones of RM-ZnO and SRM-ZnO, respectively. It can be seen clearly in Figure 3(b) and 3(c) that the surfaces of both RM-ZnO and SRM-ZnO are uneven, while the surface of SRM-ZnO is coarser with higher pore density and heterogeneity. What is noteworthy is that the raised parts of SRM-ZnO surface are connected by reticular aggregates, as shown in the red curve in Figure 3(b), which may be related to the addition of RM to seawater and these reticular aggregates may be hydrotalcite compounds. According to relevant literatures, the fine mineral particles flocculated into large agglomerates by Mg^{2+}, which also formed electrostatic bridges in seawater and acted as nucleation sites for the precipitation of hydrotalcite (Hanahan *et al.* 2004; Palmer *et al.* 2009). This finding can be confirmed by the higher content of Mg element in SRM-ZnO than RM-ZnO in Table 3. In addition, the EDS spectra taken from the surface of SRM-ZnO verify the presence of Zn element, and the distribution of Zn similar to Si, which comes from RM, suggests the even distribution of ZnO. However, the typical flake structure of ZnO could hardly be observed in SEM images of RM-ZnO and SRM-ZnO, confirming that the aggregation was prevented by RM and SRM. As can be seen from Table 3 that the weight percentage of the Zn element on SRM-ZnO is higher than RM-ZnO, which may account for the formation of hydrotalcite that can provide more adsorption sites for the loaded ZnO.

Comparison of adsorption properties between different absorbents

Figure 4 shows the differences in adsorption effects of MO by different adsorbents prepared above. The adsorption capacity of MO onto SRM is limited, indicating that the hydrotalcite compounds on SRM have poor efficiency of adsorption on MO. In addition, the removal rate of ZnO is 35.28% lower than that of RM-ZnO and even 73.18% lower than that of SRM-ZnO, indicating that ZnO plays an important role in the adsorption of RM-ZnO and SRM-ZnO. And according to the result from XRD, the size of ZnO particles on RM-ZnO and SRM-ZnO is smaller than that of ZnO, so the specific areas of RM-ZnO and SRM-ZnO are higher. RM and SRM might be appropriate for providing the suitable conditions for the growth of ZnO and hindering the aggregation of ZnO particles. The SRM-ZnO is observed distinctly to have the best effect on the adsorption of MO and get a removal ratio of 84%, indicating that the SRM-ZnO can be used to remove MO dye as adsorbent. Hydrotalcite formed in the process of seawater immersion was found in SRM-ZnO by XRD as above. The hydrotalcite compounds lost their structure and converted to Al_2O_3 and MgO during calcination of 400 °C. However, the destroyed hydrotalcite compounds on the SRM-ZnO could restore by adsorbing H_2O molecules through hydrogen bonding in the aqueous solution, which is known as the 'memory effect' (Palmer *et al.* 2009). ZnO plays a major role in the adsorption of MO onto SRM-ZnO and the hydrotalcite compounds play a secondary role that remove MO through adsorption onto its external surfaces and intercalation into its hierarchical pore network. In addition, the hydrotalcite compounds provide a larger load area for ZnO due to their hierarchical pore networks. Besides, Rath *et al.* found that the incorporation of Mg^{2+} Ca^{2+} and K^{+} from seawater into the ZnO lattice could lead to a smaller crystallite size of ZnO NPs on SRM-ZnO, which may increase the specific surface area of SRM-ZnO (Hameed *et al.* 2013; Li *et al.* 2014; Rath *et al.* 2019). Figure 3(j) and 3(k) and Table 3 show that elements Mg and K on SRM-ZnO is higher than that on RM-ZnO. The difference of Ca from Mg and K may due to that the uneven distribution of Ca in RM can lead to the measurement error of Ca. However, the effect of these metal ions on the crystallite size of ZnO on SRM-ZnO is difficult to be reflected by XRD due to the low crystallization and small content of ZnO on SRM-ZnO. According to the analysis above, the schematic diagrams of RM-ZnO and SRM-ZnO in solution are shown in Figure 5.

Table 3 | Distribution figures total spectrum

Adsorbents	Element	Wt%
RM-ZnO	Mg	0.15
	Zn	3.45
	K	0.00
	Ca	0.76
SRM-ZnO	Mg	1.37
	Zn	4.19
	K	0.11
	Ca	0.38

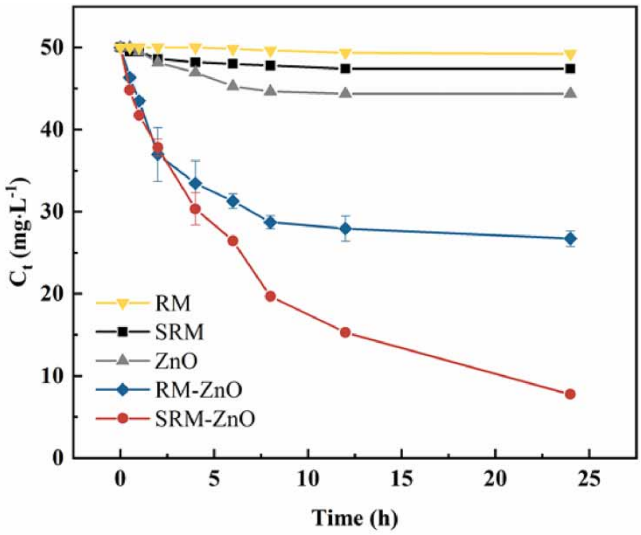

Figure 4 | Adsorption curves of MO by different adsorbents ($C_0 = 50$ mg/L, dosage = 1 g/L, pH = initial pH, temperature = 303 K).

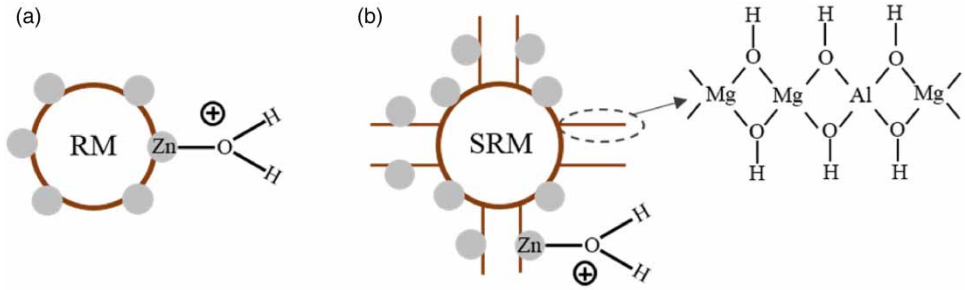

Figure 5 | Schematic diagram of RM-ZnO (a) and SRM-ZnO (b) in solution.

Influence of solution pH

The influence of pH on adsorption of MO was from pH 4 to 12, while maintaining the other parameters constant. The results depicted in Figure 6 show that the percentage of MO removal remains constant up to pH 9. The sulfonate group in the MO molecule is deprotonated to -SO_3^-, resulting in the MO molecule being negatively charged in aqueous solution. In the meanwhile, the adsorbent has a positive surface since the oxygen atoms in hydrotalcite and ZnO are protonated, which generates enhanced electrostatic attraction between MO and adsorbent. However, the removal of MO decreases at pH 10–12. On the one hand, at higher pH, more negatively charged sites existed on the surface of adsorbent, which is adverse for the adsorption of MO due to electrostatic repulsion. On the other hand, there are more OH^- ions that compete with anionic dye for the finite adsorption sites in the alkaline aqueous solution. It could also be observed from Figure 6 that the removal of MO decreases slightly at pH 4. Three major reasons could account for this phenomenon: (i) There is increased protonation of nitrogen on MO, which can weaken the electronegativity of sulfonic acid groups on MO and affect the electrostatic interactions between adsorbent and MO (Dirksen *et al.* 2002); (ii) Part dissolution of ZnO NPs may take place in acidic solution, reducing adsorption sites (Zafar *et al.* 2019); (iii) A high concentration of H^+ can prevent strong ionization of Na^+ of MO, which results in a decline in adsorption of MO. It could be obviously found that it still has adsorption capacity at pH $\geq$ 10, indicating that the electrostatic mechanism is not the only mechanism in the adsorption of MO. SRM-ZnO may also adsorb MO through hydrogen bonding or other interaction (Al-Degs *et al.* 2008; Zhang *et al.* 2014). Because the percentage of MO removal remains constant expect for low acidic pH and high alkaline pH, initial pH was chosen for future experiments.

Influence of SRM-ZnO dosage

The results about the influence of dosage on adsorption are descripted in Figure 7(a) and reveal that the removal percentage increases from 12.11% to 90.83% with the increase of adsorbent dosage. However, the higher amount of SRM-ZnO leads to

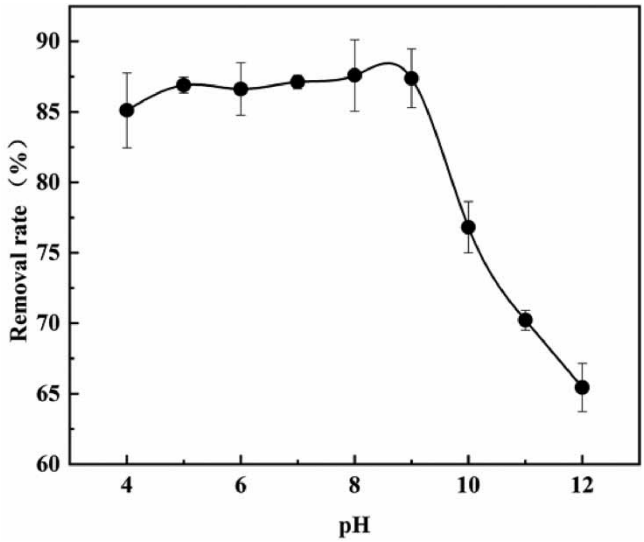

Figure 6 | Effect of pH on MO adsorption ($C_0 = 50$ mg/L, dosage = 1 g/L, temperature = 303 K, time = 24 h).

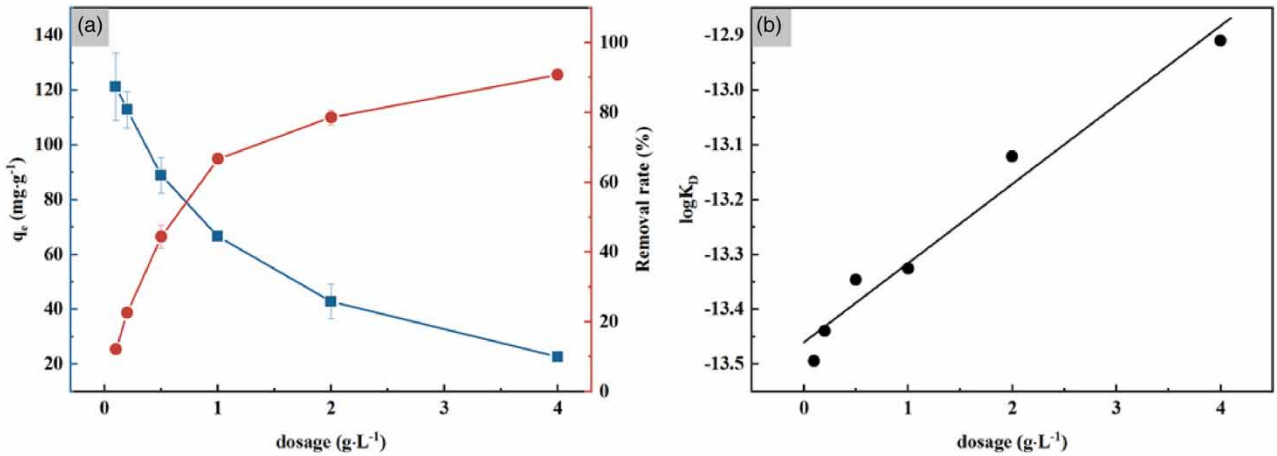

Figure 7 | Effect of dosage on adsorption and the relationship between logK$_D$ and dosage ($C_0 = 100$ mg/L, pH = initial pH, temperature = 303 K, time = 24 h).

lower adsorption capacity. This can be explained by the fact that SRM-ZnO is dispersed in the solution at a low adsorbent amount so that MO can approach the active adsorption sites easily. On the other hand, the aggregations of particles can result in overlap of adsorption sites and a decrease of the surface area of adsorbent with the increase of adsorbent amount. The surface properties of adsorbent were also studied by distribution coefficient K_D, which reflected the binding ability of the surface for an element and is expressed as Equation (13). The K_D values of a system mainly depend on pH and type of surface (Parida *et al.* 1997; Tor & Cengeloglu 2006). The K_D values for MO and SRM-ZnO at initial pH are calculated according to the following equation:

$$K_D = \frac{C_s}{C_w} \tag{13}$$

where C_s (mg/kg) is the concentration of MO in the solid particles and C_w (mg/m^3) is the equilibrium concentration of MO in the solution. As shown in Figure 7(b), K_D values increase with the increase of SRM-ZnO amount, indicating the heterogeneous surface of SRM-ZnO. It can be seen in Figure 3 that ZnO is evenly distributed on the surface of SRM-ZnO. While metal ions like Mg^{2+}, Ca^{2+} and K^+ from seawater may incorporate into ZnO lattice, resulting in a smaller crystallite

size. In addition, it is also possible that the hydrotalcite compounds formed in seawater on the surface of red mud may affect the homogeneity of SRM-ZnO.

According to the results, an excess of adsorbent can lead to a low utility of adsorption active sites. To reduce the loss of material, the subsequent study was carried out with 1 g/L of SRM-ZnO amount as the optimal dosage.

Kinetic adsorption study

The possibility of intraparticle diffusion is explained by the intraparticle diffusion model based on the intraparticle mass transfer mechanism. As shown in Figure 8(c), multilinearity is observed throughout the plots of q_t versus $t^{1/2}$, indicating that more than one step takes place in the adsorption. The slope of the initial linear portions is larger than that of the second portions at different concentrations, indicating the adsorption rate decreases with time. The first linear region is attributed to the diffusion of MO molecules to the external surface of SRM-ZnO, which is controlled primarily by boundary layer diffusion. The concentration of MO in the aqueous solution is higher than that in the solid particles in this region, providing an impetus to promote the adsorption process (Vimonses *et al.* 2009). The adsorption rate in the second linear region slows down, which is related to intraparticle diffusion within the pores of SRM-ZnO (Tajizadegan *et al.* 2016).

To explore other factors that can control the adsorption rate, the adsorption mechanism was investigated in terms of pseudo-first-order kinetics, pseudo-second-order kineticsm and Elovich kinetics. The linear curves of the pseudo-first-order, pseudo-second-order, and Elovich kinetics are shown in Figure 8(a), 8(b), and 8(d) and the relevant kinetic parameters are shown in Table 4. From the results of Table 4, the values of R^2 from the pseudo-second order kinetics are highest, indicating

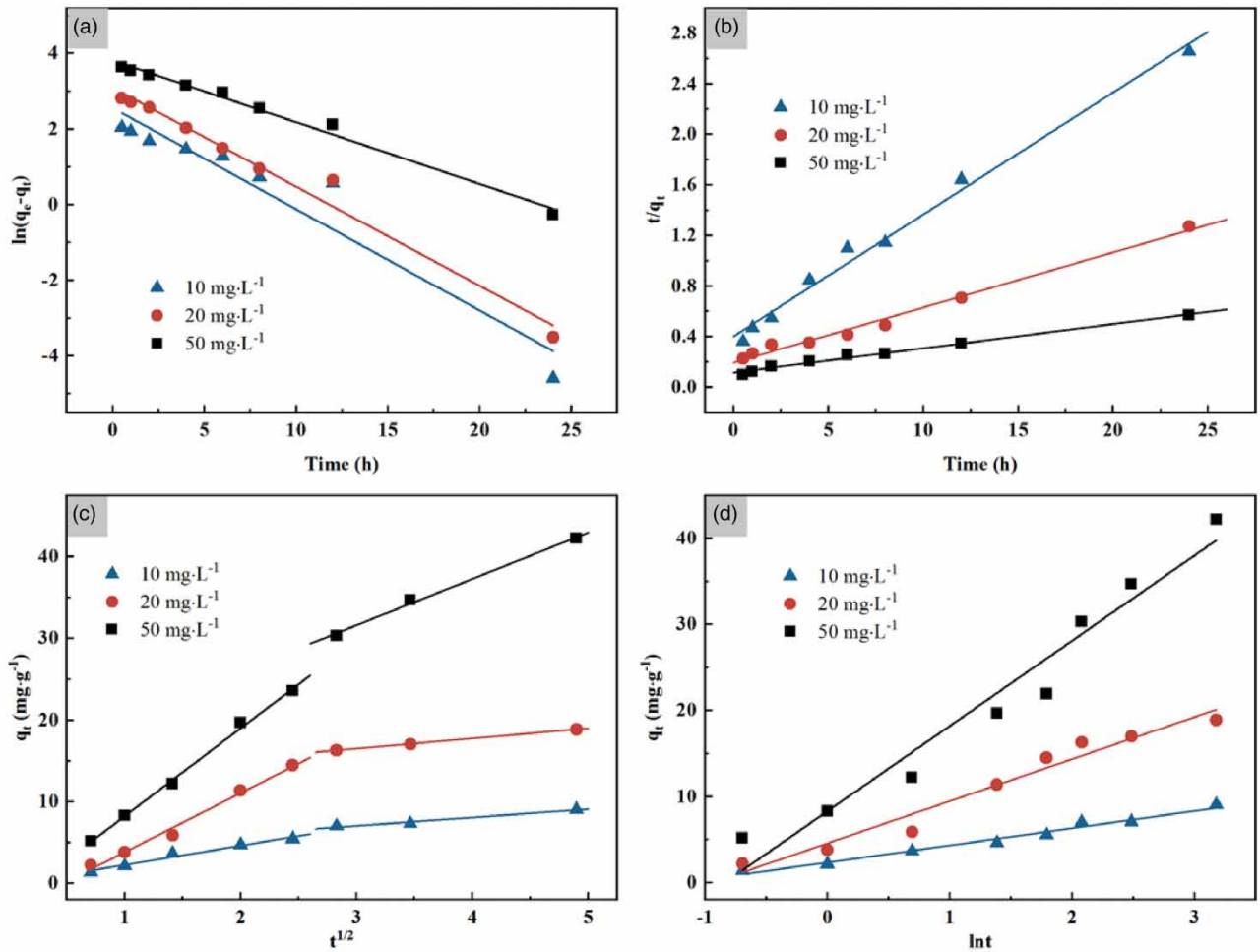

Figure 8 | The linear curves of pseudo-first-order kinetics (a), pseudo-second-order kinetics (b), intraparticle diffusion (c), and Elovich (d) models.

Table 4 | Parameters of kinetic adsorption models

		pseudo-first-order		pseudo-second-order		intraparticle diffusion		Elovich model		
C_0/mg·L^{-1}	$q_{e,\ exp}$/ mg·g^{-1}	R^2	$q_{e,\ cal}$/mg·g^{-1}	R^2	$q_{e,\ cal}$/mg·g^{-1}	R^2	I/mg·g^{-1}	R^2	a/mg·g^{-1}·h^{-1}	b/g·mg^{-1}
10	9.04	0.9222	12.92	0.9901	10.36	0.9474	3.97	0.9731	6.39	0.50
20	18.88	0.9792	22.11	0.9881	22.94	0.9958	12.74	0.9551	12.46	0.20
50	42.74	0.9880	45.30	0.9882	52.08	0.9902	14.58	0.9452	40.88	0.10

that the adsorption mechanism may maintain chemisorption (Ho 2006). However, the values of R^2 from the pseudo-second-order kinetics are also close to 1 and the values of $q_{e,\ cal}$ display a good fit with experimentally observed values of $q_{e,\ exp}$, except when the concentration is 10 mg/L, reflecting that physisorption may be one of the adsorption mechanisms. The non-conformity of values at the concentration of 10 mg/L may account for the fact that it has reached final equilibrium stage until 8 h the pseudo-first-order kinetics is normally valid over the early stage of the adsorption process. Hence, the physisorption is primary in the initial stage of the adsorption process, which is controlled chiefly by boundary layer diffusion, electrostatic effect and other physical interactions, like hydrogen bonds. And the latter stage of the adsorption process is mainly dominated by chemisorption with the control by intraparticle diffusion and chemical interaction primarily (Wanyonyi *et al.* 2014).

Adsorption isotherms

To further analyze and comprehend the mechanism, adsorption isotherms were investigated in terms of Langmuir, Freundlich, and Temkin isotherm models. The values of constants and coefficients have been summarized in Table 5. According to the results, the adsorption capacity q_e and equilibrium constants K_L, K_F, K_T, and B decrease with the rising temperature, indicating that lower temperature facilitates the adsorption and the adsorption is an exothermal process. This phenomenon may account for the fact that high temperature can promote the desorption and escape of MO molecules from the surface of SRM-ZnO (Sujana *et al.* 1998). It is also possible that adsorption can be influenced by the thermal motion of disordered molecules with the rising temperature (Yuan *et al.* 2015). However, as can be seen in Figure 9, the adsorption capacities at 303 K are close to that at 313 K, indicating that the inhibition effect of increasing temperature on adsorption is limited. The difference of R^2 represented in Table 5 shows that the Langmuir and Temkin isotherm models can elucidate the isotherm of adsorption. Furthermore, it can be seen intuitively in Figure 9 that the Temkin isotherm has more facility to display a good fit with experimental values compared with Langmuir isotherm model. These findings suggest that the adsorption perfectly complies with the Temkin isotherm model. From the Langmuir model, R_L values were calculated and found to be from 0.03 to 0.68 in the range of 0–1, demonstrating that the adsorption is favourable at all three temperatures. The $1/n$ values of the Freundlich model were observed to be in the range of 0–1, indicating that the adsorption process is under favorable adsorption conditions.

Thermodynamics

For validating the thermodynamic behaviour and determining the spontaneity of adsorption, the thermodynamic parameters were studied. The Gibbs free energy change ΔG^θ of adsorption at varying temperatures from 293 to 313 K was calculated by Equation (14). By plotting ΔG^θ against T, standard entropy ΔH^θ and standard enthalpy ΔS^θ were determined from the slope

Table 5 | Parameters of Langmuir, Freundlich, and Temkin isotherms

	Langmuir				Freundlich			Temkin		
Tempera-ture/K	q_m/mg·g^{-1}	K_L/L·mg^{-1}	R_L	R^2	K_F/mg$^{1-(1/n)}$·L$^{1/n}$·g^{-1}	$1/n$	R^2	K_T/L·g^{-1}	b_T/J·mol^{-1}	R^2
293	102.64	0.16	0.03–0.38	0.9745	26.29	0.31	0.9416	3.25	36.32	0.9902
303	92.86	0.10	0.05–0.50	0.9795	19.32	0.34	0.9428	1.73	71.62	0.9893
313	102.62	0.05	0.10–0.68	0.9945	12.23	0.43	0.9536	0.60	126.82	0.9971

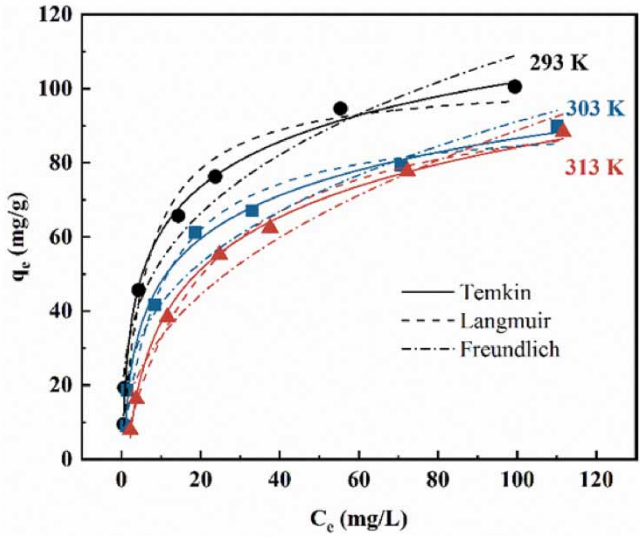

Figure 9 | Langmuir, Freundlich, and Temkin isotherm models' nonlinear fitting (dosage = 1 g/L, pH = initial pH, time = 48 h).

and intercept of the fitting line according to Equation (15), and Table 6 summarizes the values of ΔG^{θ}, ΔH^{θ}, and ΔS^{θ}.

$$\Delta G = -RT \cdot ln\frac{q_e}{C_e} \tag{14}$$

$$\Delta G = \Delta H - T \cdot \Delta S \tag{15}$$

Negative values of ΔG^{θ} show that the adsorption is spontaneous. The absolute values of ΔG^{θ} decrease with the rising temperature, indicating that the adsorption is an exothermal process with the reason that the value of ΔG^{θ} represents the magnitude of adsorption force. In addition, the absolute values of ΔG^{θ} fall in the range of 0–20 kJ·mol^{-1} for physisorption, rather than the range of 80–400 kJ·mol^{-1} for chemisorption, indicating that the adsorption is dominated by the physisorption process (Zhu *et al.* 2011). The values of $\Delta H^{\theta} < 0$ suggest that the adsorption is an exothermal process once again, and the released energy inhibits the adsorption of MO onto SRM-ZnO. Besides, the absolute value of ΔH^{θ} at 57.03 kJ·mol^{-1} does not reach the 60 kJ·mol^{-1} at which the bond breaks, confirming that the adsorption of MO onto SRM-ZnO can be defined as a physisorption process (Wang *et al.* 2019). The decrease of the standard entropy S^{θ} listed in Table 6 may accounts for the fact that the three-dimensional motion of MO molecules dispersed freely in the aqueous solution changed into the two-dimensional motion of MO molecules adsorbed on the surface of SRM-ZnO.

Influence of anions

Figure 10(a) shows the influence of different anions on adsorption of MO onto SRM-ZnO. To reduce the influence of cations and ion strength on the adsorption, sodium salt was adopted with an anion concentration of 20 mg·L^{-1}. It can be seen in Figure 10(a) that the adsorption can be affected by PO_4^{3-} and CO_3^{2-}, while the other anions (NO_3^-, SO_4^{2-}, F^-, Cl^-) have little effect on the adsorption of MO. The competition between PO_4^{3-} ions and anionic dye for occupying the adsorption sites on SRM-ZnO can disfavour the adsorption of MO dye with the reason that hydrotalcite compounds on the surface of SRM-ZnO have the adsorption capacity of PO_4^{3-} (Hanahan *et al.* 2004). In addition, a mechanism of anion exchange

Table 6 | Thermodynamic parameters

ΔG^{θ}/kJ·mol^{-1}			ΔH^{θ}/kJ·mol^{-1}	ΔS^{θ}/J·mol^{-1}·K^{-1}
293 K	303 K	313 K	− 57.03	− 171.43
− 6.72	− 5.25	− 3.29		

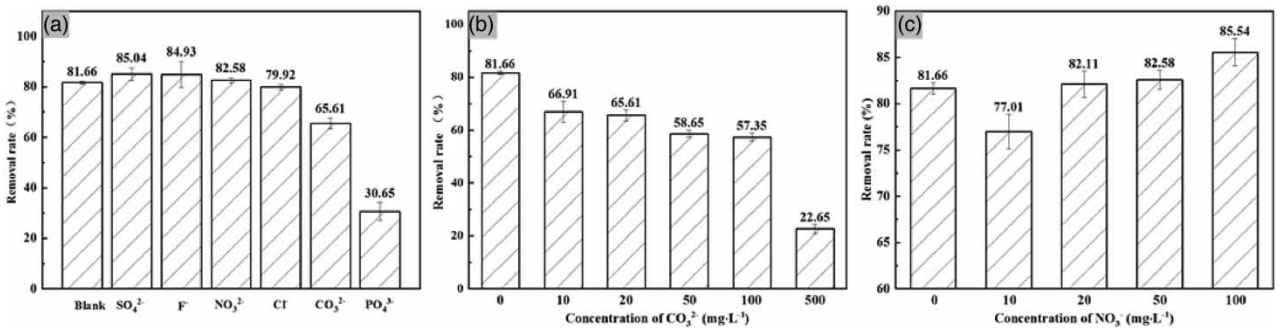

Figure 10 | Effects of different anions (a), CO_3^{2-} concentration (b) and ionic strength (c) on MO adsorption ($C_0 = 50$ mg/L, dosage = 1 g/L, pH = initial pH, temperature = 303 K, time = 24 h).

and a ranking of affinity for intercalation exist in the interlayer of hydrotalcite and the CO_3^{2-} has an exceeding preference for intercalation and prevents the exchange with other anions, so that the intercalation of CO_3^{2-} can reduce the number of adsorption sites on SRM-ZnO (Hanahan *et al.* 2004; Palmer *et al.* 2009). As can be seen in Figure 10(b) that the sorption percentage for MO decreases from 81.66% to 22.65% with an increasing concentration of CO_3^{2-}, indicating that intercalation may exist in the adsorption of MO onto SRM-ZnO. However, according to the poor adsorption effect of MO onto SRM showed in Figure 4, intercalation is not the main mechanism in the adsorption. The effect of ionic effect on the adsorption was studied by changing the concentration of NO_3^- which can reduce the impact of pH changes on adsorption. As shown in Figure 10(c), the removal rate of MO decreases in the lower ionic strength range, and then goes up with increasing ionic strength. The decreased adsorption at lower ionic strength may be attributed to the competition between NO_3^- ions and MO molecules and the increased adsorption at higher ionic strength may be explained by the hydrophobic and the aggregation of MO molecules (Liu *et al.* 2001; Al-Degs *et al.* 2008). However, the small change in removal rate indicates the poor effect of ionic strength on the adsorption of MO onto SRM-ZnO.

Adsorption mechanism

The mainly adsorption mechanism of MO by SRM-ZnO is shown in Figure 11. It can be seen from above that the adsorption of MO by SRM-ZnO is mainly dominated by physisorption, and ZnO plays the most important role in adsorption. In addition, we can find that the hydrotalcites on SRM still have a small adsorption capacity of MO from the adsorption results of MO by SRM. Oxygen atoms on ZnO and hydrotalcites tend to protonate in solution and become positive charged, which could

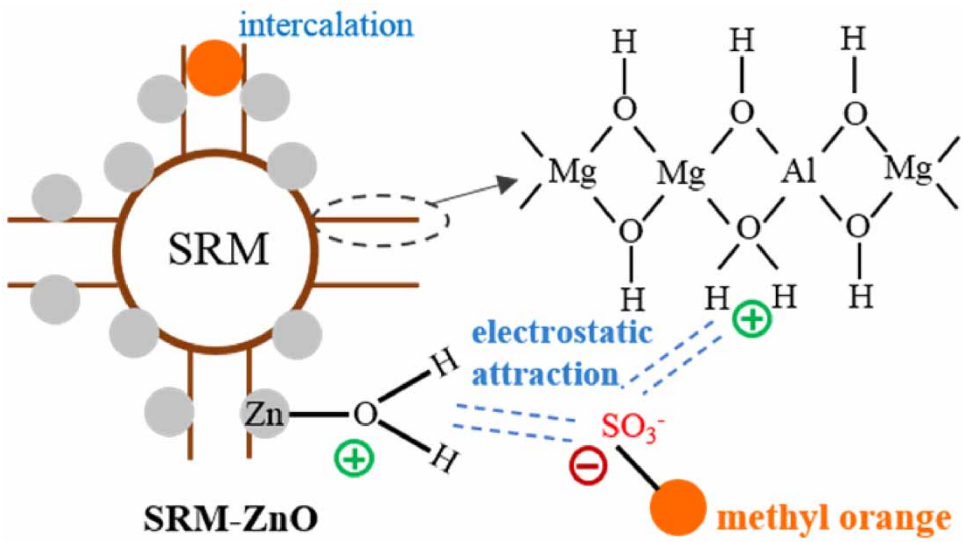

Figure 11 | The adsorption mechanism of MO by SRM-ZnO.

adsorb negative MO molecules by electrostatic attraction. Besides, the hydrotalcites on the SRM have reticular structure from SEM image. The hydrotalcites not only provide a larger load area for ZnO, but also remove some of the MO molecules by intercalation, which can be seen from the effect of CO_3^{2-} on adsorption.

CONCLUSIONS

SRM-ZnO exhibits higher adsorption capacity of MO than RM-ZnO, SRM, ZnO, and RM alone. The hydrotalcite compounds synthesized by seawater on the surface of SRM-ZnO not only improves adsorbing capacity, but also increases the surface area of red mud where more ZnO NPs could be loaded. In addition, the alkali metal ions from seawater may lead to smaller radius of ZnO atoms on SRM-ZnO, increasing the surface area of the adsorbent. The adsorption process is dominated by physisorption and supplemented with chemical adsorption. The adsorption process could be affected by PO_4^{3-} and CO_3^{2-}. Besides, the ionic strength has poor effect on the adsorption and can be explained by the hydrophobicity and aggregation of MO molecules.

SRM-ZnO provides an efficient way to recycle red mud. As shown in Table 3, the content of Zn element in SRM-ZnO is only 4.19%, indicating that there is little ZnO on SRM-ZnO, and the most of the rest is SRM. Therefore, SRM-ZnO can use little Zn element and a lot of red mud. In addition, the use of SRM is economic and can reduce the harm of red mud to the environment, and ZnO also has little harm to the environment. According to the results, SRM-ZnO is an alternative adsorbent for the removal of MO from aqueous solution and is suitable for the preparation of efficient adsorption by red mud in coastal red mud dumps.

ACKNOWLEDGEMENT

This study was funded by the Major Science and Technology Innovation Project of Shandong Province (Grant No. 2018YFJH0902) and the Taishan Scholar Foundation of Shandong Province (Grant No. tsqn201909126).

DECLARATION OF INTEREST STATEMENT

The authors declare that there is no conflict of interest regarding the publication of this paper.

DATA AVAILABILITY STATEMENT

All relevant data are included in the paper or its Supplementary Information.

REFERENCES

Ajmal, A., Majeed, I., Malik, R. N., Idriss, H. & Nadeem, M. A. 2014 Principles and mechanisms of photocatalytic dye degradation on TiO_2 based photocatalysts: a comparative overview. *RSC Advances* **4** (70), 37003–37026.

Al-Degs, Y. S., El-Barghouthi, M. I., El-Sheikh, A. H. & Walker, G. M. 2008 Effect of solution pH, ionic strength, and temperature on adsorption behavior of reactive dyes on activated carbon. *Dyes and Pigments* **77** (1), 16–23.

Ao, W., Li, J., Yang, H., Zeng, X. & Ma, X. 2006 Mechanochemical synthesis of zinc oxide nanocrystalline. *Powder Technology* **168** (3), 148–151.

Azam, K., Raza, R., Shezad, N., Shabir, M., Yang, W., Ahmad, N. & Hussain, M. 2020 Development of recoverable magnetic mesoporous carbon adsorbent for removal of methyl blue and methyl orange from wastewater. *Journal of Environmental Chemical Engineering* **8** (5), 104–220.

Chakraborty, P. & Chakrabarti, C. L. 2006 Chemical speciation of Co, Ni, Cu, and Zn in mine effluents and effects of dilution of the effluent on release of the above metals from their metal–dissolved organic carbon (DOC) complexes. *Analytica Chimica Acta* **571** (2), 260–269.

Chen, S., Kumar, R. V., Gedanken, A. & Zaban, A. 2001 Sonochemical synthesis of crystalline nanoporous zinc oxide spheres and their application in dye-sensitized solar cells. *Israel Journal of Chemistry* **41** (1), 51–54.

Dil, E. A., Ghaedi, M., Ghaedi, A. M., Asfaram, A., Goudarzi, A., Hajati, S. & Gupta, V. K. 2016 Modeling of quaternary dyes adsorption onto ZnO-NR-AC artificial neural network: analysis by derivative spectrophotometry. *Journal of Industrial and Engineering Chemistry* **34**, 186–197.

Dirksen, A., Zuidema, E., Williams, R. M., De Cola, L., Kauffmann, C., Vögtle, F. & Pina, F. 2002 Photoactivity and pH sensitivity of methyl orange functionalized poly (propyleneamine) dendrimers. *Macromolecules* **35** (7), 2743–2747.

Fernandes, J. V., Rodrigues, A. M., Menezes, R. R. & Neves, G. D. A. 2020 Adsorption of anionic dye on the acid-functionalized bentonite. *Materials* **13** (16), 3600.

Ghaedi, M., Biyareh, M. N., Kokhdan, S. N., Shamsaldini, S., Sahraei, R., Daneshfar, A. & Shahriyar, S. 2012 Comparison of the efficiency of palladium and silver nanoparticles loaded on activated carbon and zinc oxide nanorods loaded on activated carbon as new adsorbents for removal of Congo red from aqueous solution: kinetic and isotherm study. *Materials Science and Engineering: C* **32** (4), 725–734.

Gupta, V. K. & Saleh, T. A. 2013 Sorption of pollutants by porous carbon, carbon nanotubes and fullerene-an overview. *Environmental Science and Pollution Research* **20** (5), 2828–2843.

Hameed, A. S. H., Karthikeyan, C., Sasikumar, S., Kumar, V. S., Kumaresan, S. & Ravi, G. 2013 Impact of alkaline metal ions Mg^{2+}, Ca^{2+}, Sr^{2+} and Ba^{2+} on the structural, optical, thermal and antibacterial properties of ZnO nanoparticles prepared by the co-precipitation method. *Journal of Materials Chemistry B* **1** (43), 5950–5962.

Hanahan, C., McConchie, D., Pohl, J., Creelman, R., Clark, M. & Stocksiek, C. 2004 Chemistry of seawater neutralization of bauxite refinery residues (red mud). *Environmental Engineering Science* **21** (2), 125–138.

Haque, E., Lee, J. E., Jang, I. T., Hwang, Y. K., Chang, J., Jegal, J. & Jhung, S. H. 2010 Adsorptive removal of methyl orange from aqueous solution with metal-organic frameworks, porous chromium-benzenedicarboxylates. *Journal of Hazardous Materials* **181** (1–3), 535–542.

Ho, Y. 2006 Second-order kinetic model for the sorption of cadmium onto tree fern: a comparison of linear and non-linear methods. *Water Research* **40** (1), 119–125.

Hou, Q., Zhu, L., Chen, H., Liu, H. & Li, W. 2012 Growth of flower-like porous ZnO nanosheets by electrodeposition with $Zn_5(OH)_8(NO_3)_2{\cdot}2H_2O$ as precursor. *Electrochimica Acta* **78**, 55–64.

Johnston, M., Clark, M. W., McMahon, P. & Ward, N. 2010 Alkalinity conversion of bauxite refinery residues by neutralization. *Journal of Hazardous Materials* **182** (1), 710–715.

Kanade, K. G., Kale, B. B., Aiyer, R. C. & Das, B. K. 2006 Effect of solvents on the synthesis of nano-size zinc oxide and its properties. *Materials Research Bulletin* **41** (3), 590–600.

Kataria, N., Garg, V. K., Jain, M. & Kadirvelu, K. 2016 Preparation, characterization and potential use of flower shaped zinc oxide nanoparticles (ZON) for the adsorption of Victoria Blue B dye from aqueous solution. *Advanced Powder Technology* **27** (4), 1180–1188.

Keller, A. A., Wang, H., Zhou, D., Lenihan, H. S., Cherr, G., Cardinale, B. J. & Ji, Z. 2010 Stability and aggregation of metal oxide nanoparticles in natural aqueous matrices. *Environmental Science & Technology* **44** (6), 1962–1967.

Kosmulski, M. 2004 pH-dependent surface charging and points of zero charge II. Update. *Journal of Colloid and Interface Science* **275** (1), 214–224.

Lan, S., Liu, L., Li, R., Leng, Z. & Gan, S. 2014 Hierarchical hollow structure ZnO: synthesis, characterization, and highly efficient adsorption/photocatalysis toward Congo red. *Industrial & Engineering Chemistry Research* **53** (8), 3131–3139.

Lei, C., Pi, M., Jiang, C., Cheng, B. & Yu, J. 2017 Synthesis of hierarchical porous zinc oxide (ZnO) microspheres with highly efficient adsorption of Congo red. *Journal of Colloid and Interface Science* **490**, 242–251.

Li, D., Huang, J., Cao, L., OuYang, H., Li, J. & Yao, C. 2014 Microwave hydrothermal synthesis of K+ doped ZnO nanoparticles with enhanced photocatalytic properties under visible-light. *Materials Letters* **118**, 17–20.

Liu, R., Liu, X., Tang, H. & Su, Y. 2001 Sorption behavior of dye compounds onto natural sediment of Qinghe River. *Journal of Colloid and Interface Science* **239** (2), 475–482.

Liu, S., Wang, W., Cheng, Y., Yao, L., Han, H., Zhu, T. & Fu, J. 2020 Methyl orange adsorption from aqueous solutions on 3D hierarchical PbS/ZnO microspheres. *Journal of Colloid and Interface Science* **574**, 410–420.

Ma, Q. L., Xiong, R., Zhai, B. & Huang, Y. M. 2015 Ultrasonic synthesis of fern-like ZnO nanoleaves and their enhanced photocatalytic activity. *Applied Surface Science* **324**, 842–848.

Madan, S., Shaw, R., Tiwari, S. & Tiwari, S. K. 2019 Adsorption dynamics of Congo red dye removal using ZnO functionalized high silica zeolitic particles. *Applied Surface Science* **487**, 907–917.

Namasivayam, C. & Arasi, D. J. S. E. 1997 Removal of Congo red from wastewater by adsorption onto waste red mud. *Chemosphere* **34** (2), 401–417.

Orthman, J., Zhu, H. Y. & Lu, G. Q. 2003 Use of anion clay hydrotalcite to remove coloured organics from aqueous solutions. *Separation and Purification Technology* **31** (1), 53–59.

Palmer, S. J. & Frost, R. L. 2009 Characterisation of bauxite and seawater neutralised bauxite residue using XRD and vibrational spectroscopic techniques. *Journal of Materials Science* **44** (1), 55–63.

Palmer, S. J., Frost, R. L. & Nguyen, T. 2009 Hydrotalcites and their role in coordination of anions in Bayer liquors: anion binding in layered double hydroxides. *Coordination Chemistry Reviews* **253** (1–2), 250–267.

Parida, K. M., Gorai, B., Das, N. N. & Rao, S. B. 1997 Studies on ferric oxide hydroxides: III. Adsorption of selenite (SeO_3^{2-}) on different forms of iron oxyhydroxides. *Journal of Colloid and Interface Science* **185** (2), 355–362.

Rath, P. P., Behera, S. S., Priyadarshini, B., Panda, S. R., Mandal, D., Sahoo, T. & Parhi, P. K. 2019 Influence of Mg doping on ZnO NPs for enhanced adsorption activity of Congo Red dye. *Applied Surface Science* **491**, 256–266.

Rodrıguez-Paéz, J. E., Caballero, A. C., Villegas, M., Moure, C., Duran, P. & Fernandez, J. F. 2001 Controlled precipitation methods: formation mechanism of ZnO nanoparticles. *Journal of the European Ceramic Society* **21** (7), 925–930.

Shafer, M. M., Overdier, J. T., Phillips, H., Webb, D., Sullivan, J. R. & Armstrong, D. E. 1999 Trace metal levels and partitioning in Wisconsin rivers. *Water, Air, and Soil Pollution* **110** (3), 273–311.

Song, Y., Xu, J., Xu, Y., Gao, X. & Gao, C. 2011 Performance of UF–NF integrated membrane process for seawater softening. *Desalination* **276** (1–3), 109–116.

Sujana, M. G., Thakur, R. S. & Rao, S. B. 1998 Removal of fluoride from aqueous solution by using alum sludge. *Journal of Colloid and Interface Science* **206** (1), 94–101.

Tajizadegan, H., Torabi, O., Heidary, A., Golabgir, M. H. & Jamshidi, A. 2016 Study of methyl orange adsorption properties on ZnO-Al_2O_3 nanocomposite adsorbent particles. *Desalination and Water Treatment* **57** (26), 12324–12334.

Tor, A. & Cengeloglu, Y. 2006 Removal of Congo red from aqueous solution by adsorption onto acid activated red mud. *Journal of Hazardous Materials* **138** (2), 409–415.

Vimonses, V., Lei, S., Jin, B., Chow, C. W. & Saint, C. 2009 Kinetic study and equilibrium isotherm analysis of Congo Red adsorption by clay materials. *Chemical Engineering Journal* **148** (2–3), 354–364.

Wang, X., Cai, W., Liu, S., Wang, G., Wu, Z. & Zhao, H. 2013 Zno hollow microspheres with exposed porous nanosheets surface: structurally enhanced adsorption towards heavy metal ions. *Colloids and Surfaces A: Physicochemical and Engineering Aspects* **422**, 199–205.

Wang, S., Panyukov, S., Rubinstein, M. & Craig, S. L. 2019 Quantitative adjustment to the molecular energy parameter in the Lake–Thomas theory of polymer fracture energy. *Macromolecules* **52** (7), 2772–2777.

Wanyonyi, W. C., Onyari, J. M. & Shiundu, P. M. 2014 Adsorption of Congo red dye from aqueous solutions using roots of Eichhornia crassipes: kinetic and equilibrium studies. *Energy Procedia* **50**, 862–869.

Yuan, Z., Wang, Y., Han, X. & Chen, D. 2015 The adsorption behaviors of the multiple stimulus-responsive poly (ethylene glycol)-based hydrogels for removal of RhB dye. *Journal of Applied Polymer Science* **132** (28).

Zafar, M. N., Dar, Q., Nawaz, F., Zafar, M. N., Iqbal, M. & Nazar, M. F. 2019 Effective adsorptive removal of azo dyes over spherical ZnO nanoparticles. *Journal of Materials Research and Technology* **8** (1), 713–725.

Zhang, C., Yang, S., Chen, H., He, H. & Sun, C. 2014 Adsorption behavior and mechanism of reactive brilliant red X-3B in aqueous solution over three kinds of hydrotalcite-like LDHs. *Applied Surface Science* **301**, 329–337.

Zhang, J., Yan, X., Hu, M., Hu, X. & Zhou, M. 2018 Adsorption of Congo red from aqueous solution using ZnO-modified SiO_2 nanospheres with rough surfaces. *Journal of Molecular Liquids* **249**, 772–778.

Zhao, X., Li, M. & Lou, X. 2014 Sol-gel assisted hydrothermal synthesis of ZnO microstructures: morphology control and photocatalytic activity. *Advanced Powder Technology* **25** (1), 372–378.

Zhu, H. Y., Fu, Y. Q., Jiang, R., Jiang, J. H., Xiao, L., Zeng, G. M. & Wang, Y. 2011 Adsorption removal of Congo red onto magnetic cellulose/Fe_3O_4/activated carbon composite: equilibrium, kinetic and thermodynamic studies. *Chemical Engineering Journal* **173** (2), 494–502.

First received 7 December 2021; accepted in revised form 15 March 2022. Available online 24 March 2022